AIAA JOURNAL
Vol. 40, No. 7, July 2002

Nozzle Performance Modeling

Erich A. Wilson,* Dan Adler,† and Pinhas Bar-Yoseph‡
Technion—Israel Institute of Technology, 32000 Haifa, Israel

A polytropic analytical equation system for the internal flow of nozzles and ducts has been developed by a solution to the combined friction/area change compressible flow equations. Validation of the system is sought through comparison with experimental data and numerical simulations using FLUENT in the prediction of the performances of two conventional axisymmetric nozzles. Analytical performance coefficient equations have been developed from the polytropic equation system for this purpose. The predictions with consideration of nozzle divergence angle and roughness are presented for the first time. It is demonstrated that the analytical model well matches the experimental data after the throat is fully choked. The numerical and analytical results are compared and discussed. Such an analytical model is extremely useful in bridging the gap between accepted empirical parameters, such as the friction factor and performance factors, and analytical performance modeling. In aircraft nozzle simulations, where empirical data may not be available, this model provides more precise simulation capability especially applicable to modern thrust-vectoring nozzles.

Nomenclature

A	=	area, m^2
C_D	=	discharge flow coefficient
C_{fg}	=	thrust coefficient
C_v	=	velocity coefficient
C_μ, $C_{1\varepsilon}$, $C_{2\varepsilon}$	=	turbulence constants
d	=	diameter, m
$\|e\|$	=	percent error
f	=	friction factor
I	=	impulse function, N
K	=	nondimensional roughness
k	=	turbulent kinetic energy
M	=	Mach number
$\dot{m}$	=	flow rate, kg/s
p	=	pressure, Pa
p_0	=	stagnation pressure, Pa
R	=	gas constant for air, kJ · kg · K; source term for renormalization group k–ε turbulence
r	=	radius, m
S_ϕ	=	source terms
T	=	temperature, K
T_0	=	stagnation temperature, K
u, v, w	=	Cartesian velocity components, m/s
V	=	velocity, m/s
x, y, z	=	Cartesian coordinates
x^G	=	geometric expansion length, m
α	=	nozzle divergence angle, rad
β	=	nozzle convergent angle, rad
Γ	=	$\gamma(f + 2\tan\beta)/2\phi$
Γ_ϕ	=	effective transfer coefficients
γ	=	ratio of specific heats
δ	=	vectoring angle, rad
ε	=	kinetic energy dissipation rate in turbulence, J/s
	=	roughness height in roughness, m
ζ	=	$1 + (\gamma - 1)/2^* M^2$
η	=	fit term in the R source term
κ	=	analytic term, $\{2\tan(\alpha) - f[1 + (\gamma - 1)M^2]\}/\psi$; numerical von Kármán's constant
λ	=	analytic term $[(f\gamma + 2\tan\beta)/2\phi]$; numerical heat transfer coefficient
μ_e	=	effective viscosity
μ_l	=	eddy viscosity
μ_{mol}	=	molecular viscosity
μ_t	=	turbulent viscosity
ρ	=	density, kg/m^3
ϕ	=	analytic variable, $[f\gamma + (\gamma - 1)\tan\beta]$; numerical transport variable
ψ	=	$2\tan\alpha - f\gamma M^2$

Subscripts

a	=	actual
e	=	exit
i	=	isentropic, ideal
in	=	nozzle inlet
1	=	arbitrary upstream nozzle station
2	=	arbitrary downstream nozzle station

Superscripts

E	=	effective
G	=	geometric

Introduction

WITH the dawning of thrust-vectoring jet deflection technology, the nozzle design field has increased in scope and application. This technology has been well demonstrated in the F-15, F-16, F-18, and X-31 experimental as well as the F-22 and Su-37 production aircraft. Researchers are pursuing ways to both maximize thrust-vectoring nozzle effectiveness[1] in fighter aircraft and apply this technology to civil aircraft.[2]

New nozzle capabilities require more precise correlation and more seamless transitions between the current design technologies. These technologies generally include a combination of empirical, numerical, and analytical design. In reality, gaps between these methods exist that are most often compensated for by talented engineers and designers.

The dynamic requirements of thrust vectoring nozzles complicates modeling beyond the standard variables encountered with conventional nozzles.[3] One such complication is the inclusion of the variation in nozzle geometry with its influences on the jet flow.[4] Yet, as nozzle capabilities are expanded, fundamental concepts and direct correlations in nozzle performances will allow even further advancements.

Received 26 July 2000; revision received 19 June 2001; accepted for publication 13 August 2001.

*Graduate Student, Faculty of Mechanical Engineering.
†Professor and Head of the Turbomachinery Laboratory, Faculty of Mechanical Engineering.
‡Professor and Head of the Computational Mechanics Laboratory, Faculty of Mechanical Engineering.

The largest fundamental gap between design methods is the correlation between empirical performance parameters and modeling those performances through the compressible flow equations. Current practice calls for filling this gap with empirical performance coefficients that relate the calculations to actual performances. Filling this gap with an analytical solution would build a solid foundation for the future modeling of dynamic thrust-vectoring nozzles. One attempt to bridge this gap has been made[5] with less than definitive results using Young's model.[6]

A similar attempt to bridge the gap is reported by Rebolo et al.[7] They also saw the need for a more refined analytical equation model in nozzle design and development. In their development model, they obtain very good matching with experimental data, although they resorted to empirical data to adjust the ideal equations and obtain the nozzle performance prediction. A pure analytical model was not attained.

A polytropic equation system developed by the authors as a solution to the combined friction/area change compressible flow is implemented in this work. This equation system serves as a basis for the analytical equations given for the first time to predict the nozzle performance coefficients. The prediction capability of the polytropic analytical model is compared with three-dimensional numerical simulations using FLUENT and experimental data.[8]

Thus, this work seeks to bridge the gap between empirical data and system modeling by providing a purely analytical system to predict actual performances in nozzles and ducts.

Experimental Setup

Two nozzle types are used for the evaluation of the analytical model: a short-length nozzle (0.0506-m-flap-length) configuration and a long-length nozzle (0.076-m-flap-length) configuration.[8] Both nozzles have a design area ratio of $A_e/A_t = 1.35$ and a throat area of $A_t = 0.0026$ m^2. Figure 1 shows a schematic diagram of the experimental setup with the short nozzle attached.

The nozzles were machined to a maximum surface roughness of about 30 μm, and the actual surface roughness ideally reached a roughness of about 15 μm. Each nozzle was tested at various nozzle pressure ratio (NPR) values ranging from 1.5 up to 8. The discharge flow coefficient C_D and thrust coefficient C_{fg} were measured and recorded accordingly.

Analytical Model

The basic assumptions and definitions of the analytical model are presented for clarification in achieving the performance coefficients. Development of the polytropic equation system is not presented.

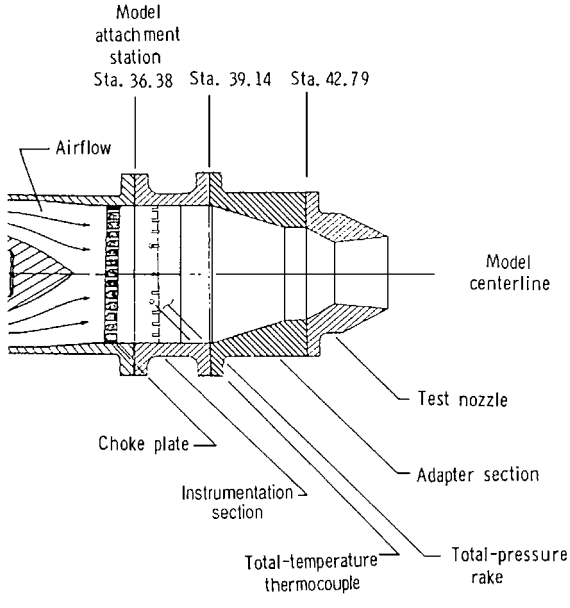

Fig. 1 Short-nozzle configuration experimental setup of Carson and Capone.[8]

Friction

To produce a robust analytical model and to enable an analytical calculation of the performance coefficients, one must consider the effects of friction through surface roughness, as well as the area change throughout the nozzle, on the jet flow.

In the case of fully developed, incompressible isothermal flow along a duct, the friction factor has an average invariant value dependent on the Reynolds number and relative roughness. The Moody diagram, created in 1944 from empirical data, is generally an acceptable graphical representation for frictional effects.

Shapiro[9] suggests that, for subsonic flows in nozzles, the Mach number dependence of the friction factor is unimportant. This is due to the relatively small gradients encountered along the nozzle length where friction has little or no effect.

In compressible flow, frictional effects are greatly complicated, and the addition of Mach number as an important dimensionless parameter must be included. For flow through the divergent sector of a nozzle, large gradients exist, and surface roughness helps to trigger and determine the position of shock and expansion waves. No definitive work on the behavior of the friction factor in convergent–divergent nozzles has been published. The usual procedure for compressible flow is to use the Moody diagram or a functional equation form, such as the Colebrook formula

$$f = \frac{0.25}{\left(\log_{10}\left[(\varepsilon/D)/3.70 + 2.51/Re\sqrt{f}\right]\right)^2} \tag{1}$$

Then, the friction factor is evaluated using the Reynolds number definition at each calculated point along the nozzle where

$$Re = \rho VD/\mu = VD/\nu \tag{2}$$

and the relative roughness ε/D. For subsonic flows, especially in ducts, the product of ρV is constant at any location along the duct, and the viscosity is evaluated as a function of the mean static temperature at a given cross section.

Polytropic Equation System

This work builds on the polytropic equation system developed by the authors and shown in Table 1. This system is created by the analytic solution to the combined compressible flow equations of friction and area change. A similar analytic solution to this system was achieved and presented by Young.[6]

Numerical Model

Calculation Method

FLUENT is a finite volume computational fluid dynamic code. The general forms of the continuity, transport, and energy equations from the Navier–Stokes equations can be written as

$$\frac{\partial(\rho\phi)}{\partial t} + \frac{\partial(\rho u\phi)}{\partial x} + \frac{\partial(\rho v\phi)}{\partial y} + \frac{\partial(\rho w\phi)}{\partial z} - \frac{\partial}{\partial x}\left(\Gamma_\phi \frac{\partial\phi}{\partial x}\right) - \frac{\partial}{\partial y}\left(\Gamma_\phi \frac{\partial\phi}{\partial y}\right) - \frac{\partial}{\partial z}\left(\Gamma_\phi \frac{\partial\phi}{\partial z}\right) = S_\phi \tag{3}$$

where the transfer coefficients Γ_ϕ, the source terms S_ϕ, and the transport variables ϕ are as given in Table 2. Additional source terms are as follows:

$$S^u = \frac{\partial}{\partial x}\left(\mu_e \frac{\partial u}{\partial x}\right) + \frac{\partial}{\partial y}\left(\mu_e\left[\frac{\partial u}{\partial y} + \frac{\partial v}{\partial x}\right]\right) + \frac{\partial}{\partial z} \times \left(\mu_e\left[\frac{\partial u}{\partial z} + \frac{\partial w}{\partial x}\right]\right) - \frac{2}{3}\frac{\partial}{\partial x}\left[\mu_e\left(\frac{\partial u}{\partial x} + \frac{\partial v}{\partial y} + \frac{\partial w}{\partial z}\right) + \rho k\right]$$

$$S^v = \frac{\partial}{\partial x}\left(\mu_e\left[\frac{\partial u}{\partial y} + \frac{\partial v}{\partial x}\right]\right) + \frac{\partial}{\partial y}\left(\mu_e \frac{\partial v}{\partial y}\right) + \frac{\partial}{\partial z} \times \left(\mu_e\left[\frac{\partial v}{\partial z} + \frac{\partial w}{\partial y}\right]\right) - \frac{2}{3}\frac{\partial}{\partial x}\left[\mu_e\left(\frac{\partial u}{\partial x} + \frac{\partial v}{\partial y} + \frac{\partial w}{\partial z}\right) + \rho k\right]$$

Table 1 Summary of differential equations and property relations for the polytropic equation system[a] of the nonsimple flow of combined area change and friction

General equation differential form	Compact differential form	Property ratios
$\frac{dM^2}{M^2} = -\frac{2\zeta}{1-M^2}\frac{dA}{A} + \frac{\gamma M^2 \zeta}{1-M^2}\frac{4f}{D}dx$	$\frac{dA}{A} = -\frac{1-M^2}{2\zeta\{1-(\gamma M^2/2)[f/\tan(\alpha)]\}}\frac{dM^2}{M^2}$	$\frac{A_2}{A_1} = \frac{M_1}{M_2}\left(\frac{\zeta_2}{\zeta_1}\right)^{(\gamma+1)\tan(\alpha)/2\phi}\left(\frac{\psi_2}{\psi_1}\right)^{[f\gamma-2\tan(\alpha)]/2\phi}$
$\frac{dV}{V} = -\frac{1}{1-M^2}\frac{dA}{A} + \frac{\gamma M^2}{2(1-M^2)}\frac{4f}{D}dx$	$\frac{dV}{V} = \frac{1}{2\zeta}\frac{dM^2}{M^2}$	$\frac{V_2}{V_1} = \frac{M_2}{M_1}\left(\frac{\zeta_1}{\zeta_2}\right)^{\frac{1}{2}}$
$\frac{dT}{T} = \frac{(\gamma-1)M^2}{1-M^2}\frac{dA}{A} - \frac{\gamma M^4(\gamma-1)}{2(1-M^2)}\frac{4f}{D}dx$	$\frac{dT}{T} = -\frac{(\gamma-1)M^2}{2\zeta}\frac{dM^2}{M^2}$	$\frac{T_2}{T_1} = \frac{\zeta_1}{\zeta_2}$
$\frac{d\rho}{\rho} = \frac{M^2}{1-M^2}\frac{dA}{A} - \frac{\gamma M^2}{2(1-M^2)}\frac{4f}{D}dx$	$\frac{d\rho}{\rho} = -\frac{M^2}{2\zeta}\frac{2\tan(\alpha)-f\gamma}{\psi}\frac{dM^2}{M^2}$	$\frac{\rho_2}{\rho_1} = \left(\frac{\zeta_1}{\zeta_2}\frac{\psi_1}{\psi_2}\right)^{[f\gamma-2\tan(\alpha)]/2\phi}$
$\frac{dP}{P} = \frac{\gamma M^2}{1-M^2}\frac{dA}{A} - \frac{\gamma M^2(1+(\gamma-1)M^2)}{2(1-M^2)}\frac{4f}{D}dx$	$\frac{dP}{P} = -\frac{\gamma M^2}{2\zeta}\kappa\frac{dM^2}{M^2}$	$\frac{P_2}{P_1} = \left(\frac{\zeta_1}{\zeta_2}\right)^{\gamma[f+2\tan(\alpha)]/2\phi}\left(\frac{\psi_1}{\psi_2}\right)^{[f\gamma-2\tan(\alpha)]/2\phi}$
$\frac{dP_0}{P_0} = -\frac{\gamma M^2}{2}\frac{4f}{D}dx$	$\frac{dP_0}{P_0} = \frac{\gamma M^2 f(1-M^2)}{2\psi\zeta}\frac{dM^2}{M^2}$	$\frac{P_{02}}{P_{01}} = \left(\frac{\zeta_2}{\zeta_1}\right)^{f\gamma(\gamma+1)/2(\gamma-1)\phi}\left(\frac{\psi_2}{\psi_1}\right)^{-[f\gamma-2\tan(\alpha)]/2\phi}$
$\frac{dT_0}{T_0} = 0$	——	$T_0 = \text{const}$
$\frac{ds}{c_p} = \frac{(\gamma-1)M^2}{2}\frac{4f}{D}dx$	$\frac{ds}{c_p} = -\frac{(\gamma-1)M^2 f}{2\zeta}\frac{1-M^2}{\psi}\frac{dM^2}{M^2}$	$\frac{\Delta s}{c_p} = \ell n\left(\left(\frac{\zeta_1}{\zeta_2}\right)^{f(\gamma+1)/2\phi}\times\left(\frac{\psi_2}{\psi_1}\right)^{[(\gamma-1)/\gamma]\{[f\gamma-2\tan(\alpha)]/2\phi\}}\right)$
$\frac{dI}{I} = \frac{1}{1+\gamma M^2}\frac{dA}{A} - \frac{\gamma M^2}{2(1+\gamma M^2)}\frac{4f}{D}dx$	$\frac{dI}{I} = -\frac{1-M^2}{1+\gamma M^2}\frac{1}{2\zeta}\frac{dM^2}{M^2}$	$\frac{I_2}{I_1} = \frac{M_2}{M_1}\left(\frac{1+\gamma M_2^2}{1+\gamma M_1^2}\right)\left(\frac{\zeta_2}{\zeta_1}\right)^{-\frac{1}{2}}$
0	$\frac{4f}{D}dx = -\frac{f}{2\zeta}\frac{1-M^2}{\psi}\frac{dM^2}{M^2}$	$\frac{4f(x_2-x_1)}{D} = \ell n\left\{\left(\frac{\zeta_2}{\zeta_1}\right)^{f(\gamma+1)/2\phi}\times\left(\frac{\psi_2}{\psi_1}\right)^{f[f\gamma-2\tan(\alpha)]/2\phi\tan(\alpha)}\left(\frac{M_1}{M_2}\right)^{f/\tan(\alpha)}\right\}$

[a]Here, $\kappa = \{2\tan(\alpha) - f[1+(\gamma-1)M^2]\}/[2\tan(\alpha) - f\gamma M^2]$, $\zeta = 1 + [(\gamma-1)/2]M^2$, $\psi = 2\tan(\alpha) - f\gamma M^2$, and $\phi = f\gamma + (\gamma-1)\tan(\alpha)$.

$$S^w = \frac{\partial}{\partial x}\left(\mu_e\left[\frac{\partial u}{\partial z}+\frac{\partial w}{\partial x}\right]\right) + \frac{\partial}{\partial y}\left(\mu_e\left[\frac{\partial v}{\partial z}+\frac{\partial w}{\partial y}\right]\right) + \frac{\partial}{\partial z}\left(\mu_e\frac{\partial w}{\partial z}\right) - \frac{2}{3}\frac{\partial}{\partial x}\left[\mu_e\left(\frac{\partial u}{\partial x}+\frac{\partial v}{\partial y}+\frac{\partial w}{\partial z}\right)+\rho k\right]$$

$$S^T = 2\mu\left[\left(\frac{\partial u}{\partial x}\right)^2 + \left(\frac{\partial v}{\partial y}\right)^2 + \left(\frac{\partial w}{\partial z}\right)^2 + \frac{1}{2}\left(\frac{\partial u}{\partial y}+\frac{\partial v}{\partial x}\right)^2 + \frac{1}{2}\left(\frac{\partial v}{\partial z}+\frac{\partial w}{\partial y}\right)^2 + \frac{1}{2}\left(\frac{\partial u}{\partial z}+\frac{\partial w}{\partial x}\right)^2\right] - \frac{2}{3}\frac{\partial}{\partial x}\left[\mu_e\left(\frac{\partial u}{\partial x}+\frac{\partial v}{\partial y}+\frac{\partial w}{\partial z}\right)+\rho k\right]$$

In addition,

$$G = \mu_e\left\{2\left[\left(\frac{\partial u}{\partial x}\right)^2 + \left(\frac{\partial v}{\partial y}\right)^2\right] + \left(\frac{\partial u}{\partial x}+\frac{\partial v}{\partial y}\right)^2\right\}$$

The total effective viscosity μ_e of the flow is

$$\mu_e = \mu_l + \mu_t \tag{4}$$

where μ_l and μ_t are the molecular and eddy viscosity, respectively. In the two-equation k–ε model of Jones and Launder,[10] the eddy viscosity is given as

$$\mu_t = C_\mu \rho k^2 / \varepsilon \tag{5}$$

In this work, the renormalization group k–ε model (RNG k–ε), similar to the standard k–ε model, but derived from a statistical technique, is used. It varies from the latter through different constant values for $C_{1\varepsilon}$ and $C_{2\varepsilon}$, otherwise $C_{1\varepsilon} = 1.44$ and $C_{2\varepsilon} = 1.72$. All other constants remain the same as the standard k–ε model.[10] The expansion of the ε equation through subtracting a new source term R from the right-hand side of Eq. (3) for turbulent diffusion ε is written as

$$R = \frac{C_\mu \rho \eta^3 (1-\eta/\eta_0)}{1+\beta\eta^3}\frac{\varepsilon^2}{k} \tag{6}$$

where $\eta = Sk/\varepsilon$, $\eta_0 \cong 4.38$, and $\beta = 0.012$. Furthermore, the effective viscosity is calculated:

$$\mu_e = \mu_{\text{mol}}\left[1 + \sqrt{(C_\mu/\mu_{\text{mol}})}\left(k/\sqrt{\varepsilon}\right)\right]^2 \tag{7}$$

which is extended to include the effects of local vorticity in swirling flows, a feature not available in the standard k–ε model.

Although most of this work is performed in the supersonic regime, nozzle performances have proven to be slightly dependent on the

Table 2 Governing numerical equations variables

ϕ	Γ	S	S_p/V	S_c/V
1 (continuity)	0	0	0	0
u	μ_e	$-\frac{\partial p}{\partial x}+S^u$	0	$S^u-\frac{\partial p}{\partial x}$
v	μ_e	$-\frac{\partial p}{\partial y}+S^v$	0	$S^v-\frac{\partial p}{\partial y}$
w	μ_e	$-\frac{\partial p}{\partial z}+S^w$	0	$S^w-\frac{\partial p}{\partial z}$
T	λ	$-p\cdot\nabla V_j+S^T$	0	$S^T-p\cdot\nabla V_j$
k	$\frac{\mu_e}{\sigma_k}$	G-$\rho\varepsilon$	$-\frac{C_\mu\rho^2 k}{\mu}$	G
ε	$\frac{\mu_e}{\sigma_\varepsilon}$	$\frac{C_{1\varepsilon}\varepsilon G-C_{2\varepsilon}\rho\varepsilon^2}{k}-R$	$-\frac{C_{2\varepsilon}\rho\varepsilon}{k}$	$\frac{C_{1\varepsilon}G}{k}$
$C_{1\varepsilon}=1.42$	$C_{2\varepsilon}=1.68$	$C_\mu=0.0845$	$\sigma_k=1.0$	$\sigma_\varepsilon=1.3$

fluid dynamics in the subsonic regime. Thus, a reversion to the inviscid Euler equations sacrifices modeling precision that could be obtained in the subsonic realm. Therefore, in an effort to test the robustness of the FLUENT code, turbulence is taken into account in this work where fully three-dimensional models are pursued.

FLUENT implements a modified law of the wall to model the effects of surface roughness. Through experimental evidence in roughened pipes, the mean velocity distribution has been determined to have the same slope, $1/\kappa$, on a semilogarithmic scale with differing intercepts, ΔB. Thus, the modified law of the wall in FLUENT is written as

$$u_p u^* \big/ (\tau_w/\rho) = (1/\kappa)\,\ell n\big[E\big(\rho u^* y_p \big/ \mu\big)\big] - \Delta B \tag{8}$$

where

$$u^* = C_\mu^{\frac{1}{4}} k^{\frac{1}{2}} \tag{9}$$

and y_p is the distance from the wall, ρ is the density, u_p is the freestream velocity, τ_w is the shear stress at the wall, and ΔB is the roughness function that quantifies the shift in the intercept due to roughness effects.

The shift in the intercept is determined automatically by the code during run time according to the roughness regime into which it falls. The roughness spectrum is divided into three regimes and met by empirical curve fits to Nikuradse's pipe roughness data by Cebeci and Bradshaw.[11] This formulation gives distinct problems in modeling the internal flow of nozzles. For this reason, a higher roughness (30 μm) was required to achieve similar results as the analytical model. This work attempted to stay within the experimental bounds, and the higher roughness value of 30 μm was needed. The divisions are as follows.

Hydrodynamically smooth ($K_s^+ < 2.25$):

$$\Delta B = 0 \tag{10}$$

Transitional ($2.25 < K_s^+ < 90$):

$$\Delta B = \frac{1}{\kappa}\,\ell n\left(\frac{K_s^+ - 2.25}{87.75} + C_{Ks}K_s^+\right)\sin\big[0.4258\big(\ell n K_s^+ - 0.8110\big)\big] \tag{11}$$

Fully rough ($K_s^+ > 90$):

$$\Delta B = (1/\kappa)\,\ell n\big(1 + C_{Ks}K_s^+\big) \tag{12}$$

where C_{Ks} is the roughness constant dependent on the type of roughness. To correspond with Nikuradse's data and with k–ε models, the roughness constant matches for pipes roughened with tightly packed, uniform sand grain with a roughness for a value of $C_{ks} = 0.5$. It is recommended to raise this value up to unity for nonuniform roughness such as represented by the presence of ribs or rivets. In this work, a uniform roughness is necessary and the roughness constant was not altered.

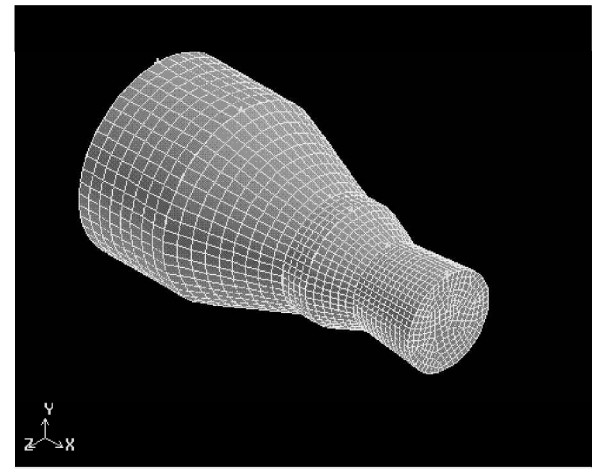

Fig. 2 Initial unstructured grid for the long-nozzle configuration of Carson and Capone.[8]

A numerical investigation using FLUENT was carried out to further validate the analytical model over the same range and conditions as the experiments were carried out. Each case was solved for a 10^{-4} convergence on all of the residuals, including continuity, momentum, energy, and turbulence. Second-order approximations for pressure with second-order upwind-based approximations for momentum, energy, and turbulence were used.

The pressure–velocity coupling was solved using the SIMPLE algorithm. This method relates the pressure to the momentum to predict the pressure field and is the most preferred method because of the low, underrelaxation factors that aid in convergence.

Turbulence

A preliminary investigation of turbulence models comparing the Reynolds stress model (RSM) with the RNG k–ε model showed that numerical deviations were only found in the fifth decimal place of the exit Mach number predicted under the same operating conditions for each model. This is viable because no significant flow separation exists in the conventional nozzles. Thus, the two-equation RNG k–ε model was chosen over the seven-equation RSM model to lower the computational requirements.

Definition of turbulence intensity and length scale was preferred on the inlet and exit boundaries of the flowfield as opposed to direct definition of the k and ε values. It was found that the exit Mach number again only varied in the fifth decimal place for intensities ranging from 0.5 to 10%. Supersonic flows in a diverging duct are not turbulent. Thus, the turbulence intensity was arbitrarily chosen to be 5%. The length scale was chosen to be $l = 0.07d$, where d is the nozzle exit diameter.

Grid

An initially uniform three-dimensional unstructured grid was used for each model with approximately 10,000 initial nodes for each nozzle configuration, as shown in Fig. 2. Throughout the computations, the grids were adapted for each case according to the velocity gradient to achieve a grid of approximately 140,000 nodes. Adaptations along the boundary allowed for proper expansion and shock wave capturing .

Performance Coefficients

In light of the development of the polytropic system, the actual performances can be estimated and compared to the ideal isentropic calculations to produce expected nozzle performance coefficients through a desired NPR range for any given nozzle design.

Flow Coefficient

The flow coefficient C_D is the ratio of the actual mass flow rate $\dot{m}_a$ at the throat of the nozzle over the ideal mass flow rate $\dot{m}_i$ at the

inlet of the nozzle. Calculating the ideal mass flow can be achieved through the inlet conditions according to

$$\dot{m}_i = \frac{p_0 A_{\text{in}} M_{\text{in}}}{\zeta_{\text{in}}^{(\gamma+1)/2(\gamma-1)}} \sqrt{\frac{\gamma}{RT_0}} \tag{13a}$$

where

$$\zeta = \{1 + [(\gamma - 1)/2]M^2\} \tag{13b}$$

Equation (13) can also be adjusted to calculate the flow rate at the throat under choking conditions. In this case it is written using the geometric throat area

$$\dot{m}_i = \frac{0.6847 p_0 A_t^G}{\sqrt{RT_0}} \tag{14}$$

Development of the polytropic flow rate is also of interest to obtain an estimation of the actual flow rate. Beginning with the flow rate equation and substituting in the ideal gas equation achieves

$$\dot{m}_a = \rho V A = \left[(p/RT) M A \sqrt{\gamma RT}\right]_2^E \tag{15}$$

where subscript 2 describes the throat location and E is for the effective values of p, M, and A. The p and T values cannot be directly related to the stagnation quantities because the system is now considered to be anisentropic. Thus, rearranging Eq. (15) and relating the p and T values back to the nozzle intlet provides

$$\dot{m}_a = p_{\text{in}} [\zeta_{\text{in}}/\zeta_2]^{\Gamma - \frac{1}{2}} [\psi_{\text{in}}/\psi_2]^{\lambda} M_2^E A_2^E \sqrt{\gamma/RT_1}$$

where

$$\psi = 2\tan\beta - f\gamma M^2, \qquad \Gamma = \frac{\gamma(f + 2\tan\beta)}{2\phi}$$

$$\lambda = \frac{f\gamma - 2\tan\beta}{2\phi}, \qquad \phi = f\gamma + (\gamma - 1)\tan\beta \tag{16}$$

where the Mach number is defined to be equal in the ideal and actual systems at the throat, the inlet pressure ratios could not be considered equivalent for both systems. With a given set of inlet conditions for both the ideal and actual cases, it is convenient to define the inlet pressure ratio to be equivalent in both systems. This allows for the static pressures and static temperatures to be equivalent at the nozzle inlet and related to the inlet stagnation pressure and stagnation temperature. This relation then provides

$$\dot{m}_a = p_0 \left[1 \Big/ \zeta_{\text{in}}^{\gamma/(\gamma-1)}\right] [\zeta_{\text{in}}/\zeta_2]^{\Gamma - \frac{1}{2}} [\psi_{\text{in}}/\psi_2]^{\lambda} M_2^E A_2^E \sqrt{\gamma \zeta_{\text{in}}/RT_0} \tag{17}$$

After the collection of terms, this is more clearly written as

$$\dot{m}_a = p_0 M_2^E A_2^E \frac{\zeta_{\text{in}}^{\Gamma - \gamma/(\gamma-1)}}{\zeta_2^{\Gamma - \frac{1}{2}}} \left[\frac{\psi_{\text{in}}}{\psi_2}\right]^{\lambda} \sqrt{\frac{\gamma}{RT_0}} \tag{18}$$

Because the inlet conditions are equivalent, it follows that the throat Mach Number achieved is unity for maximum choking. In this case, Eq. (18) for the actual flow rate can be reduced to

$$\dot{m}_a = p_0 A_2^E \frac{\zeta_{\text{in}}^{\Gamma - \gamma/(\gamma-1)}}{[1 + (\gamma - 1)/2]^{\Gamma - \frac{1}{2}}} \left[\frac{\psi_{\text{in}}}{2\tan\beta - f\gamma}\right]^{\lambda} \sqrt{\frac{\gamma}{RT_0}} \tag{19}$$

When bleeding, cooling, and leakage losses are neglected, the flow coefficient is then written

$$C_D = \frac{\dot{m}_a}{\dot{m}_i} = \left(p_0 A_2^E \frac{\zeta_{\text{in}}^{\Gamma - \gamma/(\gamma-1)}}{[1 + (\gamma - 1)/2]^{\Gamma - \frac{1}{2}}} \left[\frac{\psi_{\text{in}}}{2\tan\beta - f\gamma}\right]^{\lambda} \times \sqrt{\frac{\gamma}{RT_0}} \right) \Bigg/ \frac{p_0 A_{\text{in}} M_{\text{in}}}{\zeta_{\text{in}}^{(\gamma+1)/2(\gamma-1)}} \sqrt{\frac{\gamma}{RT_0}} \tag{20}$$

When the terms are reduced and the throat Mach is still assumed unity, Eq. (20) becomes

$$C_D = \frac{A_2^E}{A_{\text{in}} M_{\text{in}}} \frac{\zeta_{\text{in}}^{\Gamma + (1-\gamma)/2(\gamma-1)}}{[1 + (\gamma - 1)/2]^{\Gamma - \frac{1}{2}}} \left[\frac{\psi_{\text{in}}}{2\tan\beta - f\gamma}\right]^{\lambda} \tag{21}$$

which accounts for the losses through the convergent sector of the nozzle and well defines the flow coefficient. Another convenient form, when sufficient information on the convergent nozzle sector is unavailable, is to calculate both flow rates at the throat:

$$C_D = \dot{m}_a/\dot{m}_i = \left(A_t^E \Big/ A_t^G\right)\left(M_t^E \Big/ M_i\right) \zeta_t^{(\gamma+1)/2(\gamma-1) - \Gamma + \frac{1}{2}} \times \zeta_{\text{in}}^{\Gamma - \gamma/(\gamma-1)} [\psi_{\text{in}}/\psi_t]^{\lambda} \tag{22}$$

However, Eq. (22) needs to be empirically adjusted to match the experimental data. Equations (21) and (22) establish the flow coefficient as a function of the effective throat area. They are, thus, ideally suited to be implemented in thrust-vectoring nozzle design as well.

What can initially be observed throughout the development of the flow coefficient is the lack of dependance on the NPR. Though the exerimental data show that at very low-pressure ratios (NPR = 1.5) the flow coefficient is weakly dependent on the inlet pressure. Thus any estimation from this method, which now includes terms for the Mach M, roughness f, and angularity α in the nozzle will be constant regardless of the NPR.

Analytical estimation of the flow coefficient has been pursued by two methods, each relying on a different principle. Method 1 is based on Eq. (22) and requires an unrealistic adjustment to fit the data. This is an inflexible method that does not allow one to chose the nozzle geometry randomly. The advantage to this method is the independence from the convergent sector of the nozzle and is presented for this reason.

Method 2, based on Eq. (21), allows for more flexibility in the parameters. It is dependent on the geometry of the convergent sector of the nozzle. Yet no curve fitting is required to obtain a reasonable prediction. To implement method 2, a complete evaluation of the flow coefficient through calculating the various area-reduction stages in the experimental setup was not pursued. Instead, it was found that at the final stage, just before the throat, where the convergence angle is $\beta = 20$ deg, is sufficient to achieve the flow coefficient ($C_D = 0.9344$) through method 2 within about 2% of the average experimental value ($C_D = 0.9489$) for the long-nozzle configuration. Further precision is achieved through compensating for the unaccounted losses in the previous reduction stages. This is shown in the following results. The roughness for both analytical methods was $\varepsilon = 15$ μm to adhere to the actual roughness of the experimental part.

Long Nozzle C_D

Figure 3 shows the comparison of the analytical models with the numerical and experimental results for the long nozzle followed by

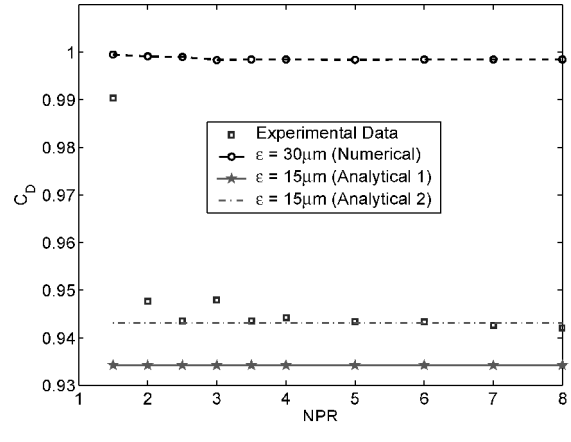

Fig. 3 Comparison of the flow coefficient estimation methods for the long-nozzle configuration.

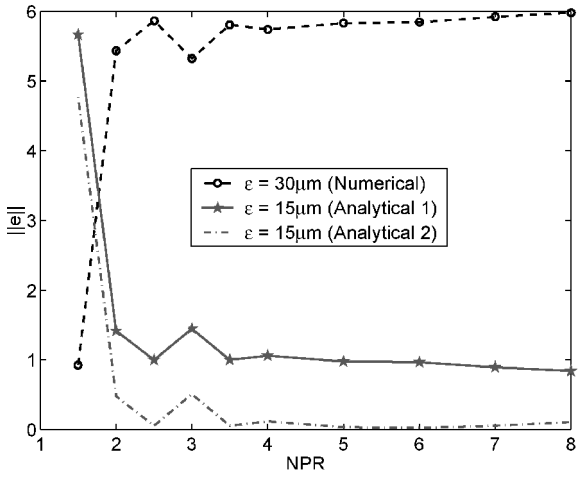

Fig. 4 Flow coefficient estimation errors for the long-nozzle configuration.

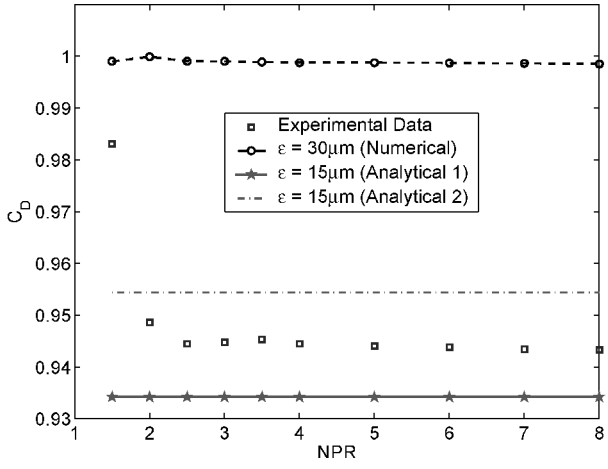

Fig. 5 Comparison of the flow coefficient estimation methods for the short-nozzle configuration.

the error analysis in Fig. 4. The best match of the experimental data is proven to be method 2 of the analytical model. The error, beyond NPR = 2 proves to be less than 0.5%. Because of the nonlinearity of the systems, this does not remain true for method 2 with the thrust coefficient, later. Method 1, the fitted method, is well adjusted with an average error of about 1.0% beyond NPR = 2.

The numerical simulations show a slight dependency on the NPR value at NPR = 1.5. Here the flow exits subsonically, and neither the analytical nor the numerical models are sensitive enough to model the experimental flow behavior. The numerical error calculation is similar to the analytical. The numerical model shows an average error of around 4% after NPR = 2 to satisfactorily emulate the experimental data.

Short Nozzle C_D

The same methodology was pursued in modeling the flow coefficient for the short nozzle configuration. The only physical difference between the two configurations is in the expansion length of the nozzle. Thus, it follows that the flow coefficient should not alter. This is the case with method 1, the fitted method, and is demonstrated in Fig. 5.

A look at the experimental results shows that this is not exactly the case in the real world. As the nozzle expansion length is shortened, the values of the flow coefficient slightly decrease at the initial NPR of 1.5. Once the exit flow is supersonic though, no noticeable difference in the flow coefficient of the experimental nozzle configurations exists.

The numerical data from the three-dimensional simulations show an unexpected trend in magnitude differences. As the expansion length is shortened, the numerical simulations show that the flow

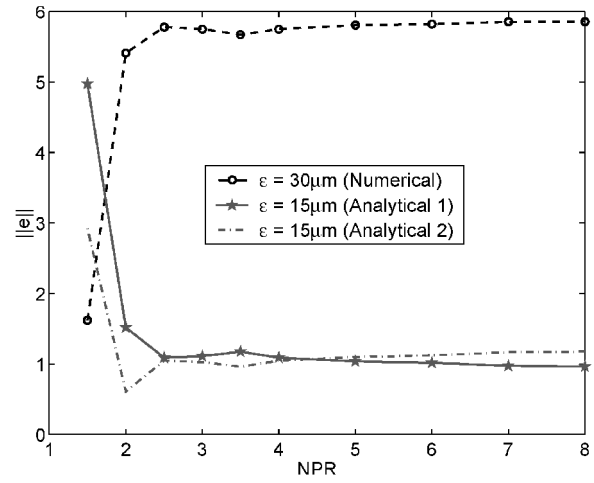

Fig. 6 Flow coefficient estimation errors for the short-nozzle configuration.

coefficient improves slightly. Numerically, the flow coefficient becomes dependent on the length of the nozzle. The shorter the nozzle length, the fewer losses are introduced into the numerical system. This dependence on nozzle length also surfaces with the analytical model method 2. Figure 5 shows a rise of about 1.0% in the flow coefficient estimation value.

If one were to assume that the expansion length has no effect on the flow coefficient, method 1 would still suffice for a good flow coefficient estimation. It proves to maintain a small error of only about 1.0% for the short nozzle, as shown in Fig. 6. The behavior of method 2 is of greater interest because it is not a curve fit, but a function of the expansion angle of the nozzle. The average error in the estimation rose slightly from 0.5 to 1.0%, well within the experimental deviation tolerance.

Comparison between the numerical simulations and the analytical models produces an interesting result. It is apparent that the numerical simulations produce a trend opposite to that of the experimental phenomena. The numerical flow coefficient is sensitive to the NPR through the transonic exit Mach values ($1.5 \leq \text{NPR} \leq 2.0$). This sensitivity is not apparent in the analytical model. On the other hand, the analytical model is better able to achieve an estimation of the actual flow coefficient in the supersonic realm ($2.0 \leq \text{NPR} \leq 8.0$).

Velocity Coefficient

The ratio of the actual exit velocity V_e to the ideal exit velocity V_{ei} is known as the velocity coefficient. This represents the effect of frictional loss in the boundary layer of the nozzle. This is difficult to determine experimentally because the losses for which it accounts are bound directly with the angularity losses as well.[12,13] However, an analytical evaluation is attainable:

$$C_v = \frac{V_e}{V_{ei}} = \frac{M\sqrt{\gamma RT}}{\left(M\sqrt{\gamma RT}\right)_i} = \frac{M}{M_i}\sqrt{\frac{\zeta_i}{\zeta}} \tag{23}$$

where the gas constant R, the ratio of specific heats γ and the stagnation temperature T_0 are considered to be constant in this adiabatic system. Thus, in the analytical model, the velocity coefficient becomes purely a function of the relation between the ideal and actual velocity values, as shown in Fig. 7.

The flow through the nozzle is underexpanded until the design point is reached. After this, the flow will be overexpanded. Thus, one can expect the velocity coefficient to have a parabolic shape with a value of unity at the design point across the NPR range. In this work, the parabolic shape of the velocity coefficient is not achieved with either in the analytical or the numerical model. The apparent underexpansion is modeled through a sensitivity before the nozzle design point of NPR = 5.1 is achieved. The performance peak is then achieved. The other side of the parabolic behavior is not attained for a lack of overexpansion sensitivity in the configuration of the models.

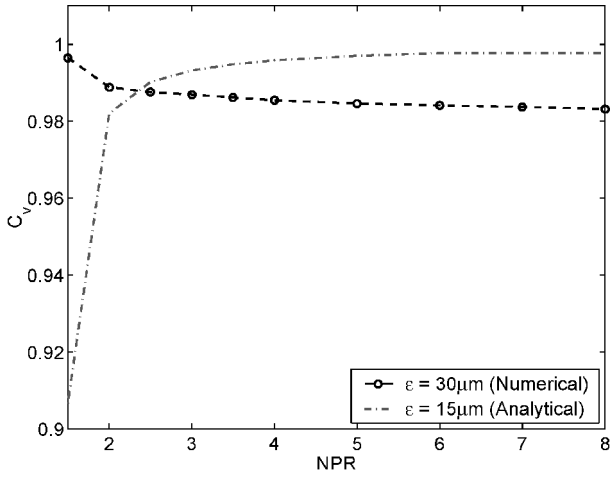

Fig. 7 Velocity coefficient for the long-nozzle configuration.

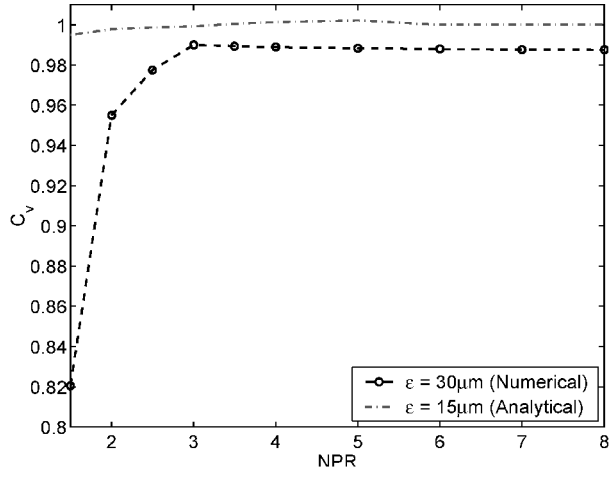

Fig. 8 Velocity coefficient for the short-nozzle configuration.

Figure 8 shows the modeling of the velocity coefficient for the short-nozzle configuration. The expected result of the similarity between the nozzle configurations is apparent.

Thrust Coefficient

The nondimensional measure of thrust, the thrust coefficient C_{fg}, is the ratio of actual to ideal thrust. For one-dimensional flow, neglecting leakage and cooling losses, it is written as follows:

$$C_{fg} = \frac{F_a}{F_i} = \frac{\dot{m}_a V_e + A_e(P_e - P_0)}{\dot{m}_i V_{ei}} \tag{24}$$

Substituting Eq. (13) and area ratio into Eq. (24) allows for an important formulation of the thrust coefficient after the terms are separated. The thrust coefficient then becomes

$$C_{fg} = \frac{A_t^E}{A_t^G} \times \left[\frac{M_a}{M_i}\sqrt{\frac{\zeta_i}{\zeta_a}} + \frac{A_e^E}{A_t^E}\frac{\sqrt{\zeta_i((\gamma+1)/2)^{(\gamma+1)/(\gamma-1)}}}{\gamma M_i}\left(\frac{p_e}{p_a} - 1\right)\right] \tag{25}$$

Equation (25) allows the thrust coefficient to be a function of the ratio between the effective and geometric areas of the throat. Although this value is unity in conventional axisymmetric nozzles, it bears significance later when the nozzle is vectored.

Figure 9 shows the capability of the analytical model, using only method 2. The error analysis is shown in Fig. 10. The analytical model succeeds in modeling the trend of the thrust coefficient.

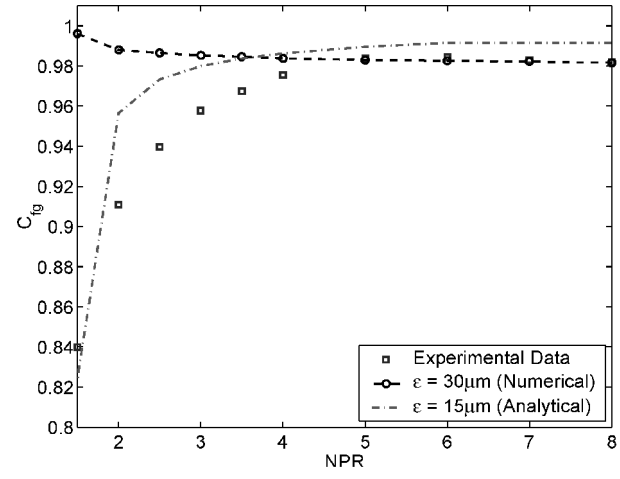

Fig. 9 Comparison of the thrust coefficient modeling for the long-nozzle configuration.

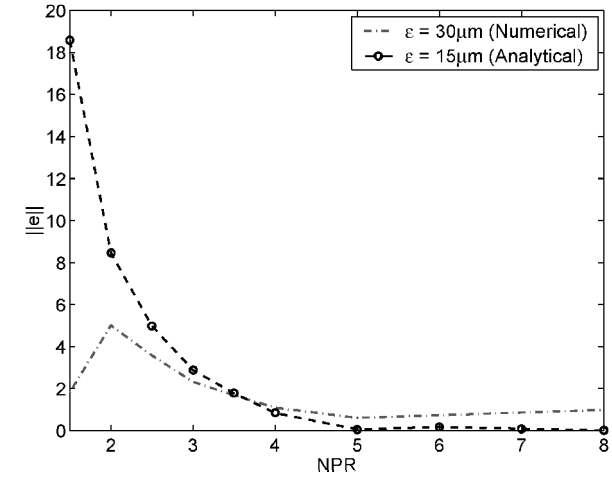

Fig. 10 Thrust coefficient error calculation for the long-nozzle configuration.

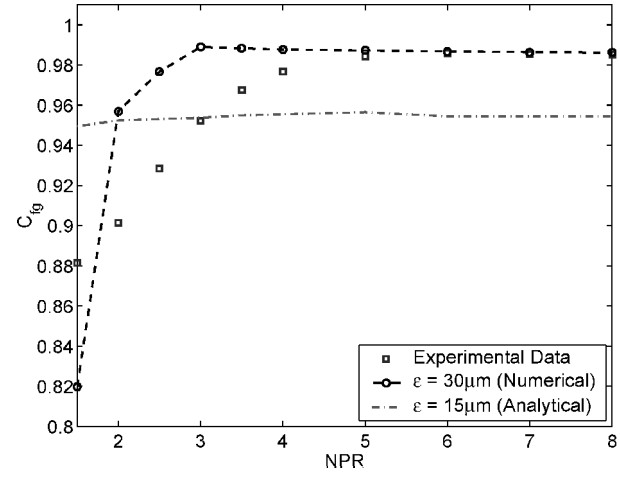

Fig. 11 Comparison of the thrust coefficient modeling for the short-nozzle configuration.

However, it is shown to overestimate the value by about 2.0% beyond NPR = 3. Even the sensitivity of the nozzle at the lower NPR levels is shown to surface in the analytical model.

The evaluation of the short-nozzle configuration shows an interesting trend in the analytical model. Figure 11 shows that the analytical model has become less sensitive as a function of the decreased nozzle length. The average error in the higher NPR values has also risen to about 4.0% as well.

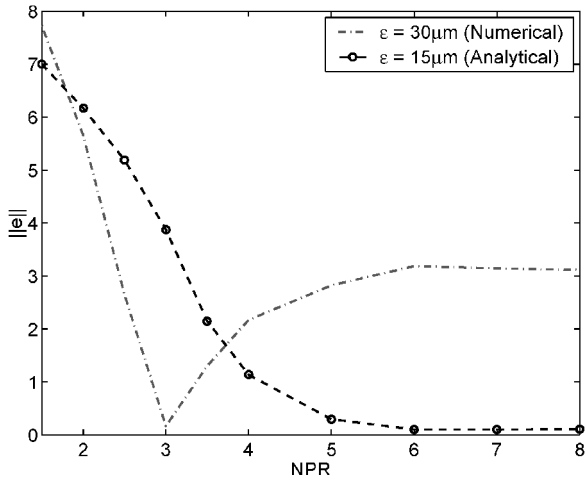

Fig. 12 Thrust coefficient error calculation for the short-nozzle configuration.

The error calculation is given in Fig. 12. This demonstrates that it is simpler to model an ideally expanded nozzle, but not impossible to model a nonideally expanded nozzle.

Conclusions

By the implementation of the polytropic equation system, an analytical model for determining the performance coefficients in axisymmetric converging–diverging nozzles has been presented. The capability of this model has been contrasted with three-dimensional simulations using FLUENT and with experimental data. It has been demonstrated that the analytical model can satisfactorily predict the nozzle performances without the need for empirical data or efficiency coefficients. The numerical simulations also proved that FLUENT is a viable and useful tool for CFD modeling in nozzle design. Through the analytical model given here not only ideal but nonideal nozzle geometries can be quickly evaluated. This system is useful in the preliminary design stage of parametric studies to determine the overall performances of a nozzle. Furthermore, this analytical model has been adjusted to allow for the modeling of thrust-vectoring nozzles.

References

[1]Chalmers, P., "Return Flight," *Mechanical Engineering*, Dec. 1999, pp. 62–64.

[2]Gal-Or, B., "Civilizing Military Thrust Vectoring Flight Control," *Aerospace America*, April 1996, pp. 20, 21.

[3]Hienz, E., Vedova, R., "Requirements, Definition and Preliminary Design for an Axisymmetric Vectoring Nozzle to Enhance Fighter Maneuverability," AIAA Paper 84-1212, 1984.

[4]Wilson, E. A., Adler, D., and Bar-Yoseph, P. Z., "Axisymmetric Thrust-Vectoring Nozzle Performance Prediction," *27th Israel International Conference on Mechanical Engineering*, Haifa, Israel, May 1998.

[5]Reynolds, M. S., Gilbert, M., and Young, F. M., "Comparison of Certain Empirical Parameters for Conical Nozzles and Diffusers with the Results of One-Dimensional Combined Change Analytical Model," *Technologies in Reactor Safety, Fluid Structure Interaction, Sloshing and Natural Hazards Engineering*, PVP-Vol. 366, American Society of Mechanical Engineers, Fairfield, NJ, 1998, pp. 309–316.

[6]Young, F. M., "Generalized One-Dimensional, Steady, Compressible Flow," *AIAA Journal*, Vol. 31, No. 1, 1993, pp. 204–208.

[7]Rebolo, R., Arrendondo, P., Matesanz, A., Velazquez, A., and Rodriguez, M., "Aerodynamics Design of Convergent–Divergent Nozzles," AIAA Paper 93-2574, 1993.

[8]Carson, G. T., and Capone, F. J., "Static Internal Performance of an Axisymmetric Nozzle with Multiaxis Thrust-Vectoring Capability," NASA TM-4237, 1991.

[9]Shapiro, A. H., *Dynamics and Thermodynamics of Compressible Fluid Flow*, Ronald, New York, 1953.

[10]Jones, W. P., and Launder, B. E., "The Prediction of Laminarization with a Two-Equation Model of Turbulence," *International Journal of Heat and Mass Transfer*, Vol. 15, 1972, pp. 301–314.

[11]Cebeci, T., and Bradshaw, P., *Momentum Transfer in Boundary Layers*, Hemisphere, New York, 1977.

[12]Mattingly, J. D., Heiser, W. H., and Daley, D. H., *Aircraft Engine Design*, AIAA Education Series, AIAA, New York, 1987.

[13]Oates, G. C., *Aerothermodynamics of Aircraft Engine Components*, AIAA Education Series, AIAA, New York, 1985.

M. Sichel
Associate Editor